Growth of surface undulations at the Rosensweig instability

Holger Knieling,[1] Reinhard Richter,[1] Ingo Rehberg,[1] Gunar Matthies,[2] and Adrian Lange[3]

[1]*Experimentalphysik V, Universität Bayreuth, D-95440 Bayreuth, Germany*

[2]*Ruhr-Universität Bochum, Universitätsstraße 150, D-44780 Bochum, Germany*

[3]*Fraunhofer Institute for Material and Beam Technology, Winterbergstraße 28, D-01277 Dresden, Germany*

We investigate the growth of a pattern of liquid crests emerging in a layer of magnetic liquid when subjected to a magnetic field oriented normally to the fluid surface. After a steplike increase of the magnetic field, the temporal evolution of the pattern amplitude is measured by means of a Hall-sensor array. The extracted growth rate is compared with predictions from linear stability analysis by taking into account the proper nonlinear magnetization curve $M(H)$. The remaining discrepancy can be resolved by numerical calculations via the finite-element method. By starting with a finite surface perturbation, it can reproduce the temporal evolution of the pattern amplitude and the growth rate. The investigations are performed for two magnetic liquids, one with low and one with high viscosity.

PACS number(s): 47.20.Ma, 47.54.−r, 75.50.Mm

I. INTRODUCTION

Plato (c. 427–347 B.C.) remarked: "You know that the beginning is the most important part of any work, especially in the case of a young and tender thing; for that is the time at which the character is being framed" [1]. The same may be true in pattern formation, which makes it most rewarding to look at its early stage. At the beginning of an evolving pattern stands an unstable mode [2]. As long as the amplitude of the mode is small, its wave number and growth rate can be calculated by linear stability analysis. In this way the early stage of pattern formation has been investigated in many different systems.

Considering interface instabilities, the Rayleigh-Taylor configuration is the most prominent example. Here the growth rate of the fastest-growing mode has been measured for granular suspensions [3] and for immiscible fluids [4]. In the latter case a monotonic, roughly linear dependence of the growth rate as a function of the density difference was derived and observed. The difficulty in setting experiments with the Rayleigh-Taylor instability is that the driving gravitational field cannot be switched on externally. This makes the preparation of a plane layer as a starting condition cumbersome.

This difficulty is eluded if the interface instability is driven by an externally applied electric or magnetic field. For an electrohydrodynamic instability of a polymer liquid/air interface the growth rate of the dominant mode was recently measured to increase with the sixth power of the reduced electrical field [5], as predicted by linear stability analysis for thin films. These thin films show a monotonic dispersion relation. However, the situation is different for thick layers, where the weight of the liquid has to be taken into account. This results in gravitational waves, leading to a nonmonotonic dispersion relation [6,7]. Neither for the electrostatic interface instability (see, e.g., ^{3}He-^{4}He mixtures [8]) nor for its magnetostatic counterpart, has the growth rate of the linearly most unstable mode been measured hitherto. In the following we fill this gap for the magnetostatic case.

The Rosensweig or normal field instability [7] is observed in a layer of magnetic fluid (MF) [10], when a critical value B_c of the vertical magnetic induction is surpassed. Figure 1 presents a photo of the final pattern of static liquid peaks, which emerge due to a transcritical bifurcation. This was investigated in theory [11–13] and experiments [14–16]. For a sudden increase of the magnetic induction B the *wave number* q_m of the fastest-growing mode was measured in the linear range, i.e., for small amplitudes [17–20]. In agreement with theory, its value increases monotonically with the supercritical magnetic induction. The growth rate of the fastest-growing mode was recently calculated in detail [21]. Here we present an experimental test of those predictions.

In order to measure the temporal evolution of the growing amplitudes, we utilize a linear array of Hall sensors [22], which is sketched together with the experimental arrangements in Sec. II. The results are compared with the outcome of the linear stability analysis in Sec. III and with numerical calculations in Sec. IV.

II. EXPERIMENT

Our experimental setup is shown in Fig. 2(a). A cylindrical vessel with an edge made of Teflon with a radius of 60 mm and a depth of 5 mm is filled to the brim with the MF and situated in the center of a Helmholtz pair of coils (for details see Ref. [19]). A camera is positioned above the vessel for optical observation. For calibration purposes, a commercial Hall probe (Group3-LPT-231) in combination with a

FIG. 1. (Color online) Rosensweig peaks of the magnetic fluid type EMG 909, Ferrotec Co., at a supercritical induction $B > B_c$ in a vessel with diameter of 120 mm. A movie showing the formation of Rosensweig patterns can be accessed at Ref [9].
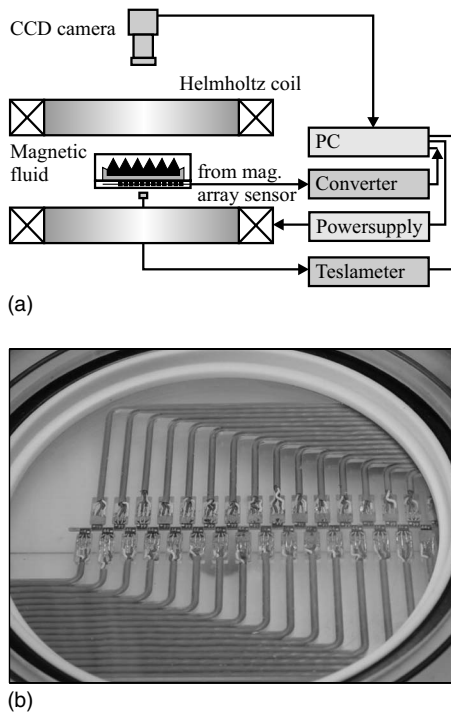
FIG. 2. Magnetic measuring principle: (a) Sketch of the experimental setup; (b) photograph of the linear array of 32 Hall sensors mounted 1.78 mm under the bottom of a transparent vessel.

digital teslameter (DTM 141) was used. For measuring the temporal evolution of the surface amplitude we take advantage of the local variation of the magnetic field, which is increased immediately beneath a magnetic spike and reduced beneath the interspike area. In order to measure these local variations, a linear array of 32 Hall sensors (KSY 44, Siemens Co.) was mounted 1.78 ± 0.1 mm below the bottom of the dish, as shown in Fig. 2(b). The sensors communicate via 32 amplifiers and a bus with the PC. Details of this method are presented in Ref. [23]. In this way line scans with a frequency up to 7 kHz are possible. This time resolution makes the method suitable for measurement of the growth rate of the pattern evolution. Although this technique is superior to the radioscopic method [24] in terms of speed, and this was our main reason for selecting it for our purposes, we should also mention its disadvantages such as the limited vertical (1 μT) and lateral (3.2 mm) resolution.

The experiments are performed with the magnetic fluids EMG 909 (Lot No. F050903B) and APG J12 (Lot No. F112795C) from Ferrotec Co. Their material parameters were measured and are as follows: a density of ρ =1005 (1097) kg m^{-3}, a surface tension of σ=2.4 $\times 10^{-2}$ (2.89×10^{-2}) N m^{-1}, and a dynamic viscosity of η =4.2×10^{-3} (51.9×10^{-3}) Pa s. The parameters of EMG 909 differ slightly from those in Ref. [19] because of a new method of fabrication of that fluid.

These two test fluids were chosen because their material parameters are rather similar, with one exception: the dynamic viscosity differs by nearly an order of magnitude. By carrying out the measurements for both fluids one can judge whether the viscosity influences the degree of agreement in a
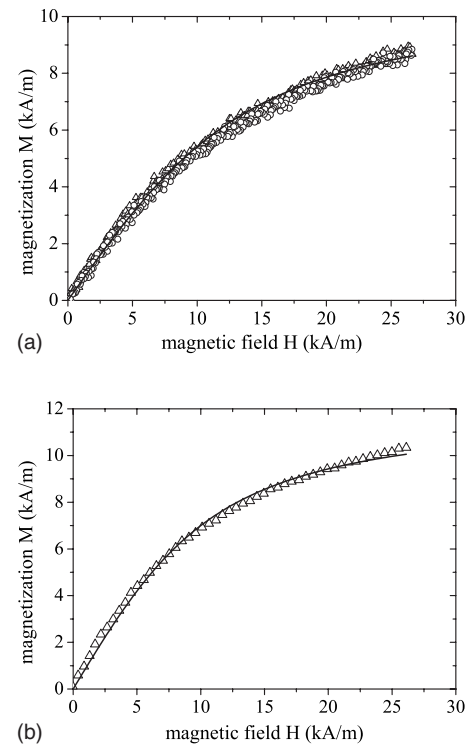

FIG. 3. Magnetization M versus the magnetic field H for the magnetic fluids EMG 909 (a) and APG J12 (b). The triangles indicate M for an increasing field, and the open circles for a decreasing field. The solid line gives the fit with the simple Langevin function (see text).

comparison between theory, numerics, and experiment with respect to the growth rate.

Furthermore, the magnetization curve $M=M(H)$ was measured (see symbols in Fig. 3). To exploit the experimental data for the theoretical calculations, the points can be fitted in the investigated range [25] with a simple Langevin function,

$$L(\alpha) = M_s^\star \left(\coth(\alpha) - \frac{1}{\alpha} \right) \quad \text{with} \quad \alpha = \frac{3\chi_0}{M_s^\star} H. \quad (2.1)$$

The best fit for EMG 909 (APG J12) yields a saturation magnetization of $M_s^\star$=10.92 (12.12) kA m^{-1} and an initial susceptibility of χ_0=0.65 (0.91) (see the solid lines in Fig. 3). Here $M_s^\star$ denotes a value that serves for a convenient description of the magnetization in the low-field regime. $M_s^\star$ differs from the true saturation magnetization M_s obtained from the entire range of magnetic fields. That range should be fitted with a more advanced function, which takes into account also the polydisperse nature of the MF (see Ref. [26], Chap. 3.8).

The data above lead to theoretical values for the critical induction [10] of $B_{c,\text{theor}}$=24.9 mT for EMG 909 and $B_{c,\text{theor}}$=20.3 mT for APG J12. The experimental values were measured as $B_{c,\text{expt}}$=25.7 (21.7) mT for EMG 909 (APG J12), which is a quite good agreement with a difference of only about 3% (6%).
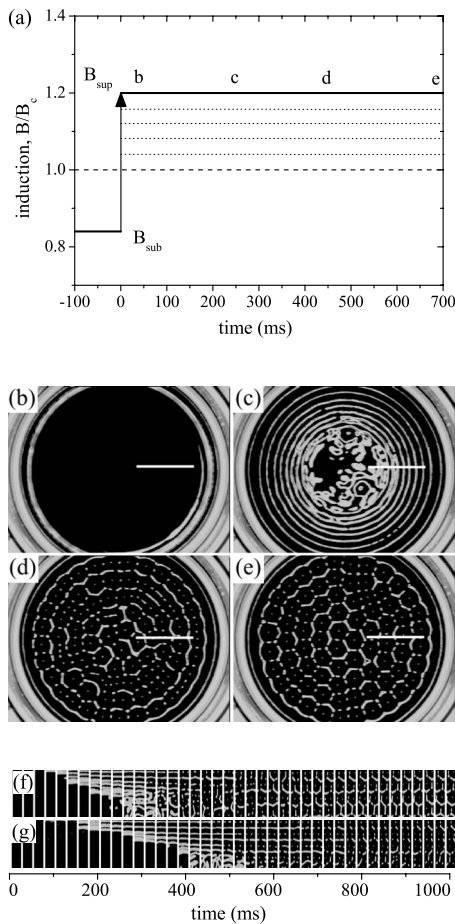
FIG. 4. Measuring the growth rate of the normal field instability. (a) Pulse sequence. The full lines display the jump from a sub- to a supercritical magnetic induction. The small letters b, c, d, and e mark the times when the pictures (b)–(e) were captured. These snapshots show the pattern at times of 40 (b), 250 (c), 450 (d), and 700 ms (e) for EMG 909. The white horizontal lines in the pictures indicate the area of measurement. (f),(g) display the pattern evolution within a small area $(8.2 \times 32.7 \ \text{mm}^2)$ around this location. (f) Presents a sequence of images for the MF mark EMG 909, and (g) the corresponding sequence for the MF mark APG J12.

On switching on the Helmholtz coils in a jumplike manner, the magnet will need a finite response time τ_B. This time depends on the size of the jump ΔB and has a maximum of $\tau_B = 30$ ms for a maximal jump of $\Delta B = 35$ mT. To reduce this time, we start all measurements from a subcritical induction of $B_{\text{sub}} = 0.84 B_c$, which leads to $\tau_B \approx 10$ ms. The other characteristic times are the capillary time $t_c = \sigma^{1/4} / (g_0^{3/4} \rho^{1/4})$ $\simeq 12.6$ (12.9) ms and the viscous time $t_\nu = \sigma / (\rho g_0 \nu)$ $\simeq 583$ (57) ms, with the fluid parameters as listed above for EMG 909 (APG J12). The kinematic viscosity ν is given by η / ρ.

Figure 4 demonstrates the utilized magnetic pulse sequence [Fig. 4(a)] and the evolution of the surface structure [Figs. 4(b)–4(g)]. As shown in Fig. 4(a), the magnetic induction is jumplike increased from a sub- to a supercritical value at time $t = 0$ ms. From Fig. 4(b) we deduce that the surface deformations first emerge at the edge of the vessel. This is
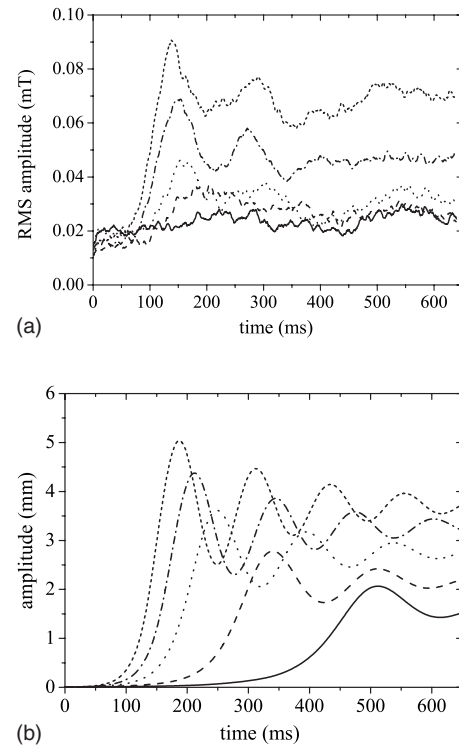

FIG. 5. Time-resolved amplitudes for the fluid EMG 909. (a) Measurements for increasing supercritical inductions $\hat{B} = 0.028$ (full line), 0.057 (dashed line), 0.100 (dotted line), 0.157 (dash-dotted line), and 0.200 (short-dashed line). For clearer appearance, the plotted lines are smoothed by averaging ten neighboring points of the original data set. (b) Numerical results for $\hat{B} = 0.028$ (full line), 0.058 (dashed line), 0.103 (dotted line), 0.153 (dashed-dotted line), and 0.203 (short-dashed line).

due to the discontinuity of the magnetic induction at this place. Because of this inhomogeneous growth of the amplitude across the vessel, the amplitude is measured only in a small region of about 35 mm between the edge and the center of the container, as marked by white horizontal lines in Figs. 4(b)–4(e). Figure 4(f) displays the evolution of the pattern from a stripelike to a hexagonal arrangement in the area of measurement. Whereas Figs. 4(b)–4(f) were recorded for the fluid EMG 909, we display in Fig. 4(g) the pattern evolution for APG J12. Its surface undergoes similar stages; only the time of appearance of those structures is different.

On the basis of the time-resolved measured data points of the sensor array, we determine the amplitude from the root-mean-square value (rms) of that data. We display the result for EMG 909 in Fig. 5(a) and for APG J12 in Fig. 6(a). For these measurements the induction was increased from the subcritical value $\hat{B} = (B - B_c) / B_c = -0.16$ to supercritical values in the interval from $\hat{B} = 0.0$ to 0.3. The offset of the amplitude results from the noise of the Hall sensors. The first phase of growth shows a dramatic increase, which is followed by an oscillatory relaxation toward the final stage in the pattern-forming process. That relaxation process differs from a purely damped sinusoidal one due to the reorganization of the peaks into a hexagonal pattern.
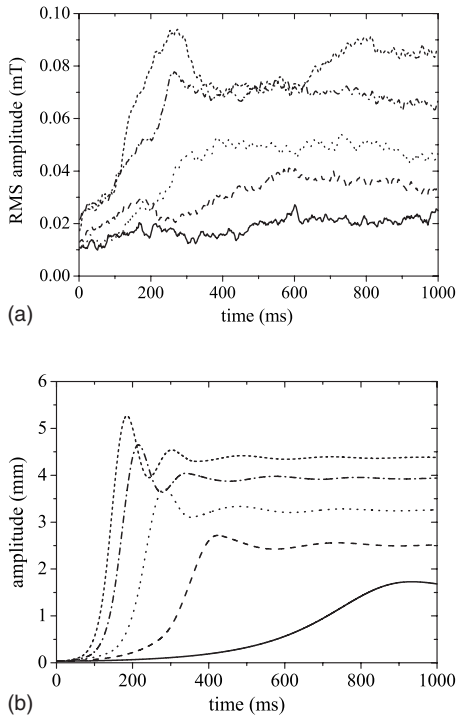
(a)

(b)

FIG. 6. Time-resolved amplitudes for the fluid APG J12. (a) Measurements for increasing supercritical inductions $\hat{B}=0.025$ (full line), 0.082 (dashed line), 0.152 (dotted line), 0.236 (dashed-dotted line), and 0.300 (short-dashed line). For clearer appearance, the plotted lines are smoothed by averaging five neighboring points of the original data set. (b) Numerical results for $\hat{B}=0.024$ (full line), 0.082 (dashed line), 0.151 (dotted line), 0.237 (dashed-dotted line), and 0.305 (short-dashed line).

The corresponding outcome of the numerical simulations (see Sec. IV) is presented in Fig. 5(b) for EMG 909 and Fig. 6(b) for APG J12. These plots show the height of the amplitude with time, as calculated before [27], but for the parameters of the investigated MF. A drastic increase of the surface height is followed by an oscillatory relaxation, in remarkable agreement with the measurements. The less viscous fluid EMG 909 goes through several oscillations after a steep increase, whereas the more viscous fluid APG J12 goes through very few oscillations.

Next we describe the extraction of the growth rate from the amplitude curves in Figs. 5(a) and 6(a). The first phase of growth in the amplitude is fitted with $y(t)=y_0+A\exp(\omega_2 t)$, where y_0 denotes an offset and A the amplitude of the exponential growth.

Due to the noisy experimental data it is difficult to determine the area of validity for the exponential growth. Therefore we adopt the following procedure. First we fit the offset y_0 of the amplitude in the range $t=[0,20]$ ms for EMG 909 ($t=[0,50]$ ms for APG J12) with a straight line without slope and hold this value constant in the following fits. Next, a series of fits of the amplitude curve with an exponential function is performed, where the end point of the fitting range is varied in the interval from $t=20$ ms to the time when the amplitude reaches its maximum. We estimate the end of the exponential range from the evolution of the fitting
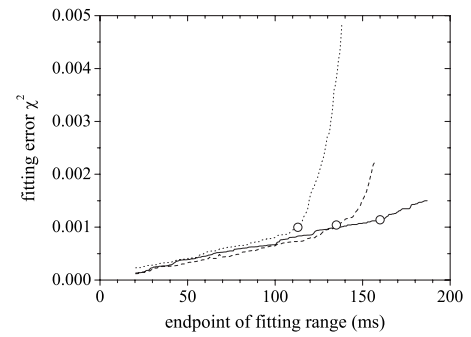

FIG. 7. Errors for fits of three amplitude curves with magnetic inductions of $\hat{B}=0.05$ (full line), 0.1 (dashed line), and 0.2 (dotted line) in dependence on the end point of the fitting range. The open circles mark the end of the fitting range.

error χ^2 according to Fig. 7. This value increases linearly as more data points are considered as long as the fitted curve is well described by an exponential function. The maximal fitting range is reached when χ^2 deviates from the linear increase and grows with a much higher rate than before. The beginning of this deviation indicates the proper fitting range for the maximal growth rate, as marked in Fig. 7 by open circles for three curves at magnetic inductions of $\hat{B}=0.05$, 0.1, and 0.2. With increasing induction the deviation from the linear growth of χ^2 becomes more prominent. The end of the fitting range estimated in this way is in accordance with the inflection point determined by visual inspection from the temporal evolution of the amplitude. The error in the growth rate resulting from the uncertainty of the fitting range was tested to be about 10% of the value of the growth rate for all applied inductions.

The measured growth rate is multiplied by the capillary time t_c yielding the dimensionless variable $\hat{\omega}_2$. The experimental values for EMG 909 (APG J12) are plotted as open squares in Fig. 8 (Fig. 9). The size of the error bars is mainly based on the uncertainty of the proper fitting range. The four lines are results of theoretical considerations which will be described in detail in the following sections.

III. COMPARISON WITH LINEAR THEORY

A. System and basic equations

A horizontally unbounded layer of an incompressible, nonconducting, and viscous magnetic fluid of thickness h and constant density ρ is considered. The fluid is bounded from below by the bottom of a container made of a magnetically impermeable material and has a free surface with air above.

In a linear stability analysis, all small disturbances from the basic state are decomposed into normal modes, i.e., into components of the form $\exp[-i(\omega t-\vec{q}\cdot\vec{r})]$, where $\vec{r}=(x,y)$ and the wave number is the absolute value of the wave vector, $q=|\vec{q}|$. With $\omega=\omega_1+i\omega_2$, the real part of $-i\omega$, ω_2, is called the growth rate and defines whether the disturbances will grow ($\omega_2>0$) or decay ($\omega_2<0$). The absolute value of the imaginary part of $-i\omega$, $|\omega_1|$, gives the angular frequency
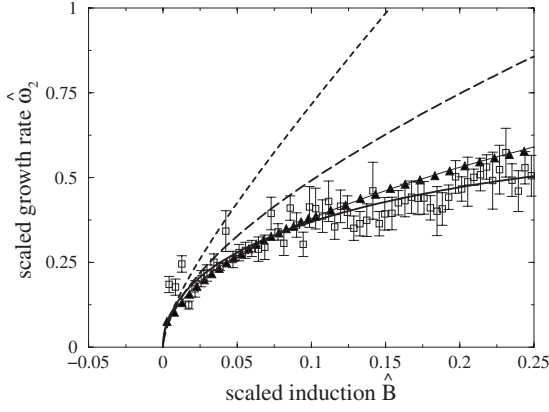
FIG. 8. Scaled growth rate $\hat{\omega}_2$ versus the scaled induction $\hat{B}$ for the magnetic fluid EMG 909. The open squares give the experimental values with the corresponding errors. A fit for those data using the approximation Eq. (3.9b) yields the thick solid line. Using a linear law of magnetization and an infinite thickness of the layer, the dashed line shows the theoretical result. The results with a nonlinear law of magnetization and a finite thickness of $h = 5$ mm are indicated by the long-dashed line. From the numerical simulations the resulting growth rate is given by the filled triangles. A fit to these results with Eq. (3.9b) gives the thin solid line.

of the oscillations if it is different from zero. With the assumption that the magnetization $\vec{M}$ of the magnetic fluid depends linearly on the applied magnetic field $\vec{H}$, $\vec{M} = (\mu_r - 1)\vec{H} = \chi\vec{H}$, the linear stability analysis leads to the dispersion relation [28–30]

$$0 = \frac{\nu^2}{\tilde{q}\coth(\tilde{q}h) - q\coth(qh)}\left(\tilde{q}[4q^4 + (q^2 + \tilde{q}^2)^2]\coth(\tilde{q}h)\right.$$
$$- q[4q^2\tilde{q}^2 + (q^2 + \tilde{q}^2)^2]\tanh(qh) - \frac{4q^2\tilde{q}(q^2 + \tilde{q}^2)}{\cosh(qh)\sinh(\tilde{q}h)}\right)$$
$$+ \tanh(qh)\left(g_0 q + \frac{\sigma}{\rho}q^3 - \frac{\mu_0\mu_r M^2}{\rho}\Lambda(qh)q^2\right), \quad (3.1)$$
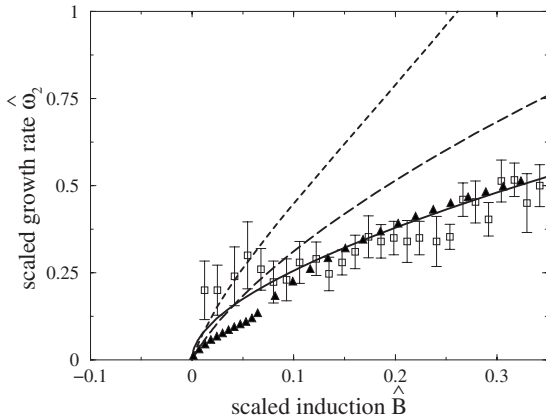

FIG. 9. Scaled growth rate $\hat{\omega}_2$ versus the scaled induction $\hat{B}$ for the magnetic fluid APG J12. The symbols and types of lines are as in Fig. 8.

where μ_r is the relative permeability of the MF, M the absolute value of the magnetization, $\vec{g}_0 = (0, 0, -g_0)$ the acceleration due to gravity, μ_0 the permeability of free space, $\tilde{q} = \sqrt{q^2 - i\omega/\nu}$, and

$$\Lambda(qh) = \frac{e^{qh}(1 + \mu_r) + e^{-qh}(1 - \mu_r)}{e^{qh}(1 + \mu_r)^2 - e^{-qh}(1 - \mu_r)^2}. \quad (3.2)$$

A nonlinear law of magnetization for a more realistic comparison with the experiment is examined, too. The magnetic part of the dispersion relation (3.1) changes to

$$(1 + \chi)M^2\Lambda(qh) \rightarrow (1 + \bar{\chi})M^2$$
$$\times\left(\frac{e^{qh(1+\bar{\chi})/(1+\chi)}(2 + \bar{\chi}) - \bar{\chi}e^{-qh(1+\bar{\chi})/(1+\chi)}}{e^{qh(1+\bar{\chi})/(1+\chi)}(2 + \bar{\chi})^2 - \bar{\chi}^2e^{-qh(1+\bar{\chi})/(1+\chi)}}\right) \quad (3.3)$$

with the differential susceptibility $\chi_d = (\partial M/\partial H)_{H_g}$, the chord susceptibility $\chi_c = (M/H)_{H_g}$, and $1 + \bar{\chi} = \sqrt{(1 + \chi_d)(1 + \chi_c)}$ at a given strength of the magnetic field H_g. With the help of the magnetization curve (see Fig. 3) one can determine χ_d, χ_c, and $\bar{\chi}$ for every supercritical induction.
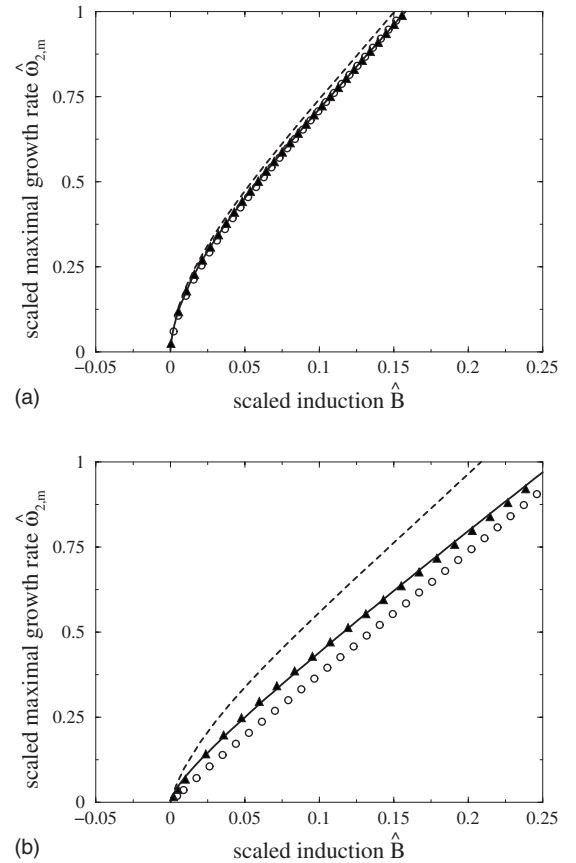

(a)

(b)

FIG. 10. Scaled maximal growth rate $\hat{\omega}_{2,m}$ versus the scaled induction $\hat{B}$ for the magnetic fluids EMG 909 (a) and APG J12 (b). Using an infinite thickness of the layer, the solid lines shows the theoretical result for EMG 909 (APG J12). The results for a finite thickness of $h = 5$ (2.5) mm are indicated by filled triangles (open circles), respectively. A calculation with $h = 5$ mm and a dynamical viscosity reduced by 50% gives the dashed lines.

The condition of marginal stability, $\omega=0$, defines the critical quantities at which the Rosensweig instability occurs. In the limit of an infinitely thick ($h\to\infty$) layer, the critical induction and the wave number, respectively, are

$$B_{c,\infty}^2 = \frac{2\mu_0\mu_r(\mu_r+1)\sqrt{\rho\sigma g}}{(\mu_r-1)^2}, \quad q_c = \sqrt{\frac{\rho g}{\sigma}}. \quad (3.4)$$

These critical values for the *onset* of the instability apply for viscous as well as for inviscid magnetic fluids.

B. Growth rate of the most unstable linear pattern for a linear law of magnetization

Within the band of unstable wave numbers, the mode with the largest growth rate is of primary importance. For its estimation it is advantageous to consider the dimensionless form (indicated by the bar) of the dispersion relation (3.1) in the limit $h\to\infty$ for growing disturbances, i.e., $\omega=i\omega_2$ with $\omega_2>0$,

$$\left(\bar{\nu}+\frac{\bar{\omega}_2}{2\bar{q}^2}\right)^2 + \frac{\bar{q}+\bar{q}^3-2\bar{B}^2\bar{q}^2}{4\bar{q}^4} - \bar{\nu}^2\sqrt{1+\frac{\bar{\omega}_2}{\bar{\nu}\bar{q}^2}} = 0. \quad (3.5)$$

All lengths were scaled with $[\sigma/(\rho g_0)]^{1/2}$, the time with $\sigma^{1/4}/(g_0^{3/4}\rho^{1/4})$, the viscosity with $\sigma^{3/4}/(g_0^{1/4}\rho^{3/4})$, and the in-

duction with $B_{c,\infty}$. The maximal growth rate is determined by $\partial\bar{\omega}_2/\partial\bar{q}=0$.

An expansion of $\bar{B}$, $\bar{q}$, and $\bar{\omega}_2$ in the form

$$\bar{B}=1+\hat{B}, \quad \bar{q}=1+\hat{q}_m, \quad \bar{\omega}_2=0+\hat{\omega}_{2,m} \quad (3.6)$$

leads to an analytical expression of the dependence of $\hat{\omega}_{2,m}$ on the induction and the viscosity. All careted quantities in (3.6) are small ($\hat{B},\hat{q}_m,\hat{\omega}_{2,m}\ll1$), and denote the scaled distances from the critical values at the onset of the instability. If $\bar{\nu}\gg\hat{\omega}_{2,m}$, Eq. (3.5) and its derivative are expanded by means of higher-order terms of the applied induction in the ansatz

$$\hat{\omega}_{2,m} = \alpha\hat{B} + \beta\hat{B}^2 + \gamma\hat{B}^3 + O(\hat{B}^4), \quad (3.7)$$

$$\hat{q}_m = \delta\hat{B}^2 + \epsilon\hat{B}^3 + O(\hat{B}^4). \quad (3.8)$$

The dependence of the maximal growth rate on the parameters viscosity and induction is then given by [21]

$$\hat{\omega}_{2,m} = \begin{cases} \dfrac{2}{\bar{\nu}}\hat{B} + \left(\dfrac{1}{\bar{\nu}}-\dfrac{3}{\bar{\nu}^3}\right)\hat{B}^2 + \left(\dfrac{10}{\bar{\nu}^5}-\dfrac{3}{\bar{\nu}^3}\right)\hat{B}^3 & \text{for } 0\le\hat{B}<\bar{\nu}^2/6, & (3.9a) \\[2ex] c_1\sqrt{\hat{B}}+c_2\hat{B} & \text{for } \bar{\nu}^2/6\ll\hat{B}\le0.4. & (3.9b) \end{cases}$$

For scaled inductions larger than $\bar{\nu}^2/6$, one has to solve the full implicit dispersion relation (3.1) and its derivative with respect to q numerically. The fit for an excellent agreement with these numerical data includes a linear term and a square-root term with respect to $\hat{B}$, where the coefficients depend on the magnetic fluid.

The calculation of the scaled induction, which separates the two scaling regimes in Eq. 3.9, gives $\bar{\nu}^2/6\simeq8\times10^{-5}$ ($\simeq9\times10^{-3}$) for the fluid EMG 909 (APG J12). Therefore Eq. (3.9b) has to be used for most practical experiments because such supercritical inductions above B_c can hardly be accomplished in an experiment. Using the test fluids EMG 909 and APG J12, respectively, the fit of the maximal growth rate results in the coefficients $c_1\simeq1.39$ and $c_2\simeq2.77$ for EMG 909 [31] and $c_1\simeq0.45$ and $c_2\simeq2.97$ for APG J12. The corresponding curves are plotted as solid lines in Figs. 10(a) and 10(b), respectively.

Next we test the robustness of the theoretical curve against variations of the experimental parameters. Taking into account the finite thickness of the layer does not create much difference if the test fluid is EMG 909: neither a thickness of $h=5$ mm (filled triangles) nor of $h=2.5$ mm (open circles) causes much change, as shown in Fig. 10(a). Figure 10(b) displays that for the fluid APG J12 only the smallest

tested thickness of 2.5 mm results in an apparent difference in comparison to the case of an infinite thickness. Additionally to the experimental filling level of 5 mm, the height of 2.5 mm had been chosen because the inevitable field gradient at the edge of the vessel can diminish the fluid level in the central part by up to a factor of 0.6 [19].

During the course of the experiment an increase of the temperature of the MF may occur. Therefore a hypothetical reduction of the dynamic viscosity η by 50% at a filling level of $h=5$ mm is considered in order to test its influence. The results are indicated by the dashed lines in Fig. 10 and show a noticeable influence on the maximal growth rate only in the case of the fluid APG J12. All in all, the theoretical behavior seems to be rather robust to variations of the experimental parameters.

IV. COMPARISON OF THEORETICAL AND EXPERIMENTAL RESULTS

The comparison starts with the values for EMG 909. The measured growth rates (see Fig. 8, open squares) can be fitted using the approximation (3.9b) which is marked by the thick solid line in Fig. 8. It results in the coefficients $c_{1,\text{expt}}$

TABLE I. List of critical inductions B_c and fit coefficients c_1 and c_2 for EMG 909 and APG J12. The theoretical, numerical, and experimental data were fitted according to Eq. (3.9b), where c_1 scales the square-root term and c_2 the linear term.

	B_c (mT)	c_1	c_2
EMG 909			
Experiment	25.7	1.44	−0.87
Theory, $M(H)$ linear[a]	20.1	1.39	2.77
Theory, $M(H)$ nonlinear[b]	24.9	1.24	0.94
Numerics	25.0	1.23	−0.10
APG J12			
Experiment	21.7	0.69	0.32
Theory, $M(H)$ linear[a]	17.3	0.45	2.97
Theory, $M(H)$ nonlinear[b]	20.4	0.47	1.45
Numerics	21.9		

[a]The linear stability theory uses a linear function to fit the magnetization.

[b]The linear stability theory uses the Langevin function to fit the magnetization.

$\simeq 1.44$ and $c_{2,\text{expt}} \simeq -0.87$. The dashed line shows the result for a linear law of magnetization, i.e., the numerical solution of the dispersion relation (3.1) and its derivative with respect to q, and an infinite thickness of the layer. Applying again a fit according to Eq. (3.9b) yields $c_{1,\text{theor,lin}} \simeq 1.39$ and $c_{2,\text{theor,lin}} \simeq 2.77$. Comparing these two curves and the corresponding fit coefficients (see also Table I), it becomes clear that these theoretical values differ grossly from the measured ones.

In Sec. III B we saw that taking into account a finite layer thickness or a variation of the viscosity of the MF has only a diminutive influence, and therefore cannot much reduce the difference with the experimental data. Thus a nonlinear law of magnetization is examined for a more appropriate comparison. Using the actually measured material data, a finite layer thickness of $h=5$ mm, and the magnetization curve of Fig. 3(a) results in the data plotted by the long-dashed line. The latter, which can be fitted by Eq. (3.9b) using $c_{1,\text{theor,nlin}} \simeq 1.24$ and $c_{2,\text{theor,nlin}} \simeq 0.94$, lies appreciably closer to the experimental data.

Figure 9 shows the experimental (open squares) and the theoretical results for the second tested magnetic fluid, APG J12. A fit of the experimental data by means of Eq. (3.9b) gives the thick solid line, where the fit coefficients are given in Table I. The theoretically determined growth rates are based on either a linear law for the magnetization (dashed line) or a nonlinear one (long-dashed line).

In contrast to previous studies [18,19], a nonlinear law of magnetization is necessary in order to reduce the gap between the theoretical data for the maximal growth rate and the experimental results. Despite that, for $\hat{B}=0.25$ the theoretical value thus estimated is about 70% (EMG 909) and 35% (APG J12), respectively, above the measured one.

One may discuss several reasons for the considerable disagreement between theory and experiment, such as errors in the material parameters or a limited resolution of the sensor
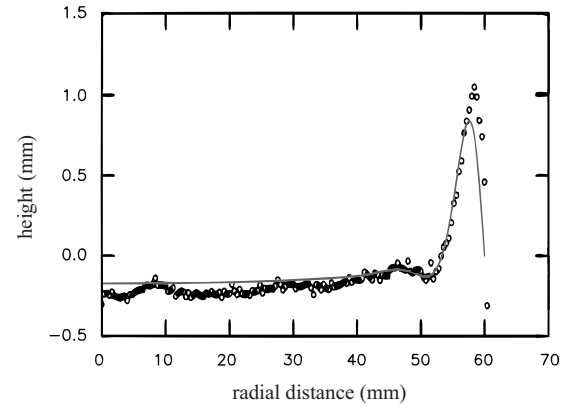

FIG. 11. Radioscopic measured surface profile (circles) of the fluid EMG 909 recorded for $\hat{B}=-0.1$ for a fluid height of 3 mm. At the position of 0 mm is the center, at 60 mm the inner edge of the Teflon vessel. The y axis denotes the height of the fluid with respect to its level without a magnetic field.

array. However, most importantly a systematic deviation may have its origin in the finite size of the container: because of that, experiment and theory may have different starting conditions. Figure 11 displays a radioscopic surface profile recorded for $\hat{B}=-0.1$, i.e., in a subcritical region of the instability. One clearly sees surface undulations well before the critical induction. They are most prominent next to the edge of the vessel and have their origin in the discontinuity of the magnetization at this place. Thus, the experiment will start with a finite disturbance whereas the theory is estimated for a infinitesimal perturbation.

In the following we perform numerical calculations starting with a finite perturbation, in order to test whether this can better describe the experimental data.

V. NUMERICAL SIMULATIONS

Our numerical simulations are based on a coupled system of nonlinear governing equations: the Maxwell equations in the magnetic liquid and its surroundings, the Navier-Stokes equations in the magnetic liquid, and the Young-Laplace equation on the free surface.

Because magnetic fluids can be regarded as insulators, the Maxwell equations in the entire space are given by

$$\text{curl } \vec{H} = \vec{0}, \quad \text{div } \vec{B} = 0, \tag{4.1}$$

with the constitutive relation

$$\vec{B} = \begin{cases} \mu_0(\vec{M} + \vec{H}) & \text{in } \Omega_F(t), \\ \mu_0 \vec{H} & \text{outside } \Omega_F(t), \end{cases}$$

where $\Omega_F(t)$ denotes the domain that is occupied by the magnetic liquid at time t. The magnetization $\vec{M}$ is assumed to follow a Langevin law [see Eq. (2.1)]. Such a nonlinear law results in a better approximation of the measured magnetization than a linear dependence of $\vec{M}$ on $\vec{H}$ as used in Sec. III.

The hydrodynamic behavior of the magnetic liquid is described by the nonstationary, incompressible Navier-Stokes

equations in the time-dependent fluid domain $\Omega_F(t)$. These equations read as follows:

$$\rho\left(\frac{\partial\vec{u}}{\partial t} + (\vec{u}\cdot\vec{\nabla})\vec{u}\right) = \text{div } \mathbb{T}(\vec{u},p,\vec{H}) - \rho\vec{g}_0z, \qquad (4.2a)$$

$$\text{div } \vec{u} = 0. \qquad (4.2b)$$

Here, $\vec{u}$ denotes the fluid velocity, p the sum of the hydrodynamic pressure and the fluid-magnetic pressure, and $\mathbb{T}$ the magnetically augmented stress tensor with

$$\mathbb{T}_{ij}(\vec{u},p,\vec{H}) = \eta\left(\frac{\partial u_i}{\partial x_j} + \frac{\partial u_j}{\partial x_i}\right) - \left(p + \frac{\mu_0}{2}H^2\right)\delta_{ij} + B_iH_j.$$

The system of equations is completed by the force balance at the free surface, which is given by the Young-Laplace equation in the following form:

$$[\mathbb{T}(\vec{u},p,\vec{H})\vec{n}] = \sigma\mathcal{K}\vec{n}, \qquad (4.3)$$

where σ is the surface tension, $\vec{n}$ the outer unit normal on $\partial\Omega_F(t)$, and $\mathcal{K}$ the sum of the principal curvatures. Here, $[\psi]$ denotes the jump of the quantity ψ across the interface. Furthermore, the kinematic condition

$$\vec{u}\cdot\vec{n} = v_\Gamma \qquad (4.4)$$

with the normal velocity v_Γ of the free surface Γ_F is used. Finally, the system is closed with initial and boundary conditions.

In order to solve the coupled system of nonlinear partial differential equations numerically, it is split into two subproblems: a magnetostatic problem for the magnetic field and a flow problem which also involves the Young-Laplace equation.

We consider for our numerical simulations a bounded three-dimensional domain $\tilde{\Omega} = \tilde{G} \times (\tilde{z}_b, \tilde{z}_t)$ with a two-dimensional hexagonal base $\tilde{G}$ which contains exactly one peak. Furthermore, the interval $(\tilde{z}_b, \tilde{z}_t)$ in the $\tilde{z}$ direction is chosen such that its end points are far below and above the free surface, respectively. This ensures that the position of the free surface does not affect the magnetic field on the upper and lower boundaries.

The Maxwell equations are transformed into their dimensionless form by using the strength of the applied magnetic field and a characteristic length scale l, which is a fixed multiple of the wavelength of the pattern. In this way, the domain $\Omega = G \times (z_b, z_t)$ is obtained. The Maxwell equations in dimensionless form read

$$\text{curl } \vec{H} = \vec{0}, \quad \text{div } \vec{B} = 0 \quad \text{in } \Omega. \qquad (4.5)$$

The first differential equation in (4.5) ensures the existence of a scalar magnetostatic potential φ such that $\vec{H} = -\vec{\nabla}\varphi$. Hence, by using the second differential equation of (4.5), we get

$$-\text{div}[\mu(\vec{x},|\vec{\nabla}\varphi|)\vec{\nabla}\varphi] = 0 \quad \text{in } \Omega. \qquad (4.6)$$

The coefficient function $\mu(\vec{x},H)$ is given by

$$\mu(\vec{x},H) = \begin{cases} 1 & \vec{x} \in \Omega_A(t), \\ 1 + \dfrac{M(H)}{H} & \vec{x} \in \Omega_F(t), \end{cases}$$

where $\Omega_F(t)$ and $\Omega_A(t)$ are the three-dimensional subdomains of Ω that correspond to the areas inside and outside the magnetic liquid at time t, respectively. Equation (4.6) is equipped with boundary conditions which correspond to the case of a flat surface. We refer to [16] for details.

The solution of the magnetostatic problem (4.6) is approximated by a finite-element method with continuous, piecewise triquadratic functions. The nonlinearity in (4.6) due to the nonlinear magnetization law is overcome by a fixed-point iteration. In each iteration step, the large system of linear equations arising is solved by a geometric multigrid method.

For solving the time-dependent Navier-Stokes equations, we start with a semidiscretization in time by applying the fractional-step ϑ-scheme [32,33], which is of second order and strongly A-stable [34,35]. The resulting equations in each time step are solved by a finite-element method which incorporates the Young-Laplace equation (4.3). Furthermore, the arbitrary Lagrangian Eulerian (ALE) approach is applied to handle the time-dependent fluid domains.

It is well known that the finite-element spaces which are used to approximate velocity and pressure in the discretized Navier-Stokes equations cannot be chosen independently but have to satisfy a constraint that is given by the inf-sup (or Babuška-Brezzi) condition. We used in our calculations continuous, piecewise, triquadratic functions for the velocity and discontinuous, piecewise, linear functions of the pressure. This pair of spaces satisfies the inf-sup condition [36,37].

After discretizing the Navier-Stokes equations in time and space, one has to solve in each time step a nonlinear saddle-point problem. The nonlinearity is resolved by a fixed-point iteration. The resulting system of linear equations is again solved by a geometric multigrid method. We refer to Refs. [38–40] for details.

The position of the free surface is updated after each time step by using the kinematic condition (4.4). Since the domain that is occupied by the magnetic liquid changes in time, the meshes used by both finite-element methods have also to change in time in order to guarantee that the free surface is approximated by faces of three-dimensional mesh cells. We have used a simple algebraic mesh update which arranges the mesh points according to the height of the free surface position.

All numerical results were obtained by using the software package MOONMD [41].

In order to get the developed surface profile, one has to choose a proper initial surface perturbation. Starting with a completely flat surface ($z \equiv 0$), the calculations will result in the same flat surface for all times, independent of the strength of the applied magnetic field. We used a rotationally symmetric cosinelike profile as initial perturbation. Its amplitude was selected as 0.007 mm (0.034 mm) for the fluid EMG 909 (APG J12), respectively. Figure 12 demonstrates for the fluid EMG 909 that higher (lower) starting values
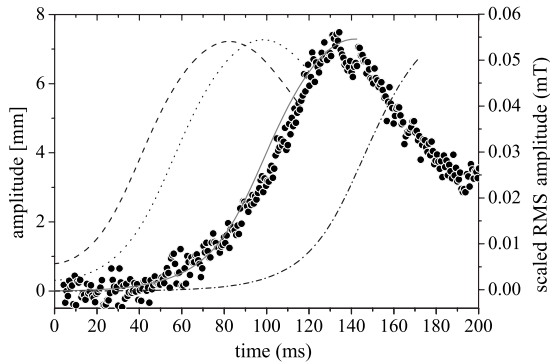
FIG. 12. Temporal evolution of the measured peak amplitude for $\hat{B}=0.25$ for the MF EMG 909 (dots) and the corresponding evolution of the calculated peak amplitude for different initial perturbation heights of 0.791 (dashed line), 0.313 (dotted line), 0.007 (full line), and 0.001 mm (dashed-dotted line). The scaled rms amplitude is the measured rms amplitude minus its offset at 0 ms.

result in an earlier (later) growth of the perturbation in comparison with the experimental curve. The selected perturbation gives the expected dynamic growth of the perturbation into the oscillatory relaxation process, provided the strength of the applied field is large enough. Note that the obtained dynamic growth rate is independent of the initial perturbation height.

It has been shown in theory and experiment that the wave number of maximal growth depends linearly on the scaled magnetic induction $\hat{B}$ [18]. For a first attempt to unravel the mismatch between theory and experiment, we performed all numerical calculations with the critical wavelength q_c.

From these numerical simulations, we obtain a critical value for the onset of the Rosensweig instability by taking the smallest value that results in a growth of the perturbation. If the strength of the applied field is smaller than this obtained threshold, then the initial surface perturbation declines toward a flat surface. The sets of critical inductions for the two fluids are collected in the second row of Table I.

Also, from numerical simulations it is possible to determine the growth rate. Due to the lack of noise, the fitting range for the exponential growth of the amplitude can be easily determined via the maximum of the numerical differentiated amplitude curve. The resulting values of the growth rate at different supercritical inductions are indicated by filled triangles in Figs. 8 and 9. Fitting these numerical results for the fluid EMG 909 with Eq. (3.9b) results in the coefficients $c_{1,num} \simeq 1.23$ and $c_{2,num} \simeq -0.1$ (see the thin solid line). Due to the structure of the numerical results for the fluid APG J12, we refrained from a single fit over the entire range of $\hat{B}$. Therefore no fit coefficients $c_{1,num}$ and $c_{2,num}$ for APG J12 are given in the corresponding list (Table I).

VI. DISCUSSION AND CONCLUSIONS

We performed measurements of the growth of surface undulations at the Rosensweig instability for different supercritical inductions, applied to two magnetic fluids of different viscosity. Comparing the values of the growth rates for both tested magnetic fluids (cf. Table I), one notes that the less viscous one (EMG 909) has larger growth rates than the more viscous one (APG J12). At $\hat{B}=0.25$ the experimental value of $\hat{\omega}_{2,m}$ for EMG 909 is about 18% larger than the corresponding value for APG J12. That the less viscous fluid grows faster is intuitively clear since less viscosity goes along with less friction inside the fluid. Therefore more energy is transformed into the movement of the fluid, which appears in our case as the growth of the peaks.

A comparison of experimental and theoretical values (cf. Figs. 8 and 9) shows that the theoretical values, obtained from calculations with a linear magnetization curve, overestimate the experimental ones considerably. This mismatch could be reduced by taking into account the proper nonlinear magnetization curve in the linear theory. Even so, the estimated growth rates remained 70% (35%) above the experimental values for the less (more) viscous fluid, respectively. There are several reasons for this discrepancy.

First we do not measure the growth of only the fastest-growing mode, but an averaged growth of several modes, by using the rms value of the measured amplitude from the Hall-sensor array. In contrast to the case of the static, tilted field instability [22], we could not fit the spatial modulation of the signal of the sensor array with periodic functions. This difficulty might stem from the higher complexity of the evolving pattern which cannot fully be captured by a one-dimensional array, and the limited spatial resolution of the array. As an outcome we are not able to estimate a dispersion relation $\omega_2(q)$, as in Refs. [3,42]. Therefore the growth rate extracted from the rms values of the magnetic amplitude data can only be considered a rough estimate for a maximal growth rate determined from the dispersion relation.

Second, the vessel in the experiment has a finite size, which causes an inhomogeneous growth of the surface amplitude starting with a *finite amplitude* from the edge of the vessel. In contrast, the theory is for a laterally infinite layer of fluid and infinitesimal surface perturbations. We could corroborate this thesis with radioscopic measurements of the static surface profile, unveiling a finite surface elevation for subcritical inductions.

Here the numerical simulation via the finite-amplitude method comes to the rescue, because it can take a starting condition with finite amplitude into account. The calculated temporal evolution of the surface undulations agrees well with the measurement, including the oscillations, which were observed for two different viscosities. This feature is beyond the framework of a linear stability analysis and can be calculated only with the help of numerical methods [27]. More importantly, the numerically estimated growth rates match the measured ones well. For supercritical inductions of $\hat{B} \leq 0.1$, the agreement between experimental and numerical values is clearly better for the less viscous fluid EMG 909. The two data sets can hardly be distinguished. For supercritical inductions of $\hat{B} > 0.1$, the agreement between experimental, numerical, and theoretical values is clearly better for the more viscous fluid APG J12. The numerical results fall practically onto the fit of the experimental ones (compare filled triangles and thick solid line in Fig. 9).

Remaining discrepancies between experiment and numerics may stem from the following. Due to computational costs, so far the numerical simulations were performed for a pattern with fixed, critical wavelength q_c for all values of the magnetic induction. In future, more refined calculations will take into account the linear dependence $\omega_2(q)$ for the wave number of maximal growth. Furthermore, in the experiment first circular ridges appear, which then arrange in a hexagonal pattern during their growth. This might change the growth rate, in contrast to the numerical evolution, which starts already with a hexagonal pattern. This latter point is difficult to solve numerically.

For future experiments the finite amplitude at the beginning of the experiment should be reduced, e.g., by introducing a ramp as in Ref. [16]. More importantly it will be necessary to reduce, to the highest possible extent, the effect of the lateral boundaries on the growth of the unstable mode by choosing improved experimental and computational conditions (e.g., size of the container). Moreover, we expect an improvement of the accuracy by a radioscopic measurement of the growth rate with a two-dimensional x-ray detector [24], so that it becomes feasible for slow evolution of highly viscous magnetic fluids. A Fourier analysis of these spatiotemporally resolved surface profiles will allow an estimation of the growth rate of the fastest-growing mode.

To conclude, we have experimentally, theoretically, and numerically investigated the growth rate during the first stage of pattern formation in the Rosensweig instability. Despite the use of a nonlinear law of magnetization, there remains a discrepancy between the predictions of linear stability analysis and experimental data. In contrast, the experimental data are confirmed by numerical simulations using a nonlinear magnetization curve together with a finite initial surface undulation. The growth behavior of the related electrostatic instability should be similar, but remains to be investigated.

[1] *Columbia World of Quotations*, edited by R. Andrews, M. Biggs, and M. Seidel (Columbia University Press, New York, 1996), Quotation No. 44484.

[2] M. C. Cross and P. C. Hohenberg, Rev. Mod. Phys. **65**, 851 (1993).

[3] C. Völtz, W. Pesch, and I. Rehberg, Phys. Rev. E **65**, 011404 (2001).

[4] P. Carles, Z. Huang, G. Carbone, and C. Rosenblatt, Phys. Rev. Lett. **96**, 104501 (2006).

[5] K. A. Leach, Z. Lin, and T. P. Russel, Macromolecules **38**, 4868 (2005).

[6] G. I. Taylor and A. D. McEwan, J. Fluid Mech. **22**, 1 (1965).

[7] M. D. Cowley and R. E. Rosensweig, J. Fluid Mech. **30**, 671 (1967).

[8] M. Wanner and P. Leiderer, Phys. Rev. Lett. **42**, 315 (1979).

[9] D. Castellvecchi, http://focus.aps.org/story/v15/st18

[10] R. E. Rosensweig, *Ferrohydrodynamics* (Cambridge University Press, Cambridge, U.K., 1985).

[11] A. Gailitis, J. Fluid Mech. **82**, 401 (1977).

[12] R. Friedrichs and A. Engel, Phys. Rev. E **64**, 021406 (2001).

[13] R. Friedrichs and A. Engel, Europhys. Lett. **63**, 826 (2003).

[14] J.-C. Bacri, and D. Salin, J. Phys. (France) Lett. **45**, L767 (1984).

[15] R. Richter and I. V. Barashenkov, Phys. Rev. Lett. **94**, 184503 (2005).

[16] C. Gollwitzer, G. Matthies, R. Richter, I. Rehberg, and L. Tobiska, J. Fluid Mech. **571**, 455 (2007).

[17] B. Abou, J. Wesfreid, and S. Roux, J. Fluid Mech. **416**, 217 (2000).

[18] A. Lange, B. Reimann, and R. Richter, Phys. Rev. E **61**, 5528 (2000).

[19] B. Reimann, R. Richter, I. Rehberg, and A. Lange, Phys. Rev. E **68**, 036220 (2003).

[20] A. Lange, R. Richter, and L. Tobiska, Mitt. Ges. Angew. Math. Mech. **30**, 171 (2007).

[21] A. Lange, Europhys. Lett. **55**, 327 (2001).

[22] B. Reimann, R. Richter, H. Knieling, R. Friedrichs, and I. Rehberg, Phys. Rev. E **71**, 055202(R) (2005).

[23] B. Reimann, Ph.D. thesis, University of Bayreuth, Shaker Verlag, Aachen, 2003.

[24] R. Richter and J. Bläsing, Rev. Sci. Instrum. **72**, 1729 (2001).

[25] J. Browaeys, J.-C. Bacri, C. Flament, S. Neveu, and R. Perzynski, Eur. Phys. J. B **9**, 335 (1999).

[26] R. Richter and A. Lange, in *Recent Developments in Ferrofluid Research*, edited by S. Odenbach, Lecture Notes in Physics (Springer, Berlin, to be published).

[27] G. Matthies and L. Tobiska, J. Magn. Magn. Mater. **289**, 346 (2005).

[28] J. Weilepp and H. R. Brand, J. Phys. II **6**, 419 (1996).

[29] B. Abou, G. N. de Surgy, and J. E. Wesfreid, J. Phys. II **7**, 1159 (1997).

[30] H. W. Müller, Phys. Rev. E **58**, 6199 (1998).

[31] Due to the measurement of the material data of the actual lot of EMG 909, the values of c_1 and c_2 differ from those given in Ref. [21].

[32] M. Bristeau, R. Glowinski, and J. Periaux, Comput. Phys. Rep. **6**, 73 (1987).

[33] R. Glowinski, *Handbook of Numerical Analysis* (North-Holland, Amsterdam, 2003), Vol. IX, pp. 3–1176.

[34] P. Klouček and F. S. Rys, SIAM J. Numer. Anal. **31**, 1312 (1994).

[35] S. Müller-Urbaniak, Ph.D. thesis, Heidelberg University, 1993.

[36] V. Girault and P.-A. Raviart, *Finite Element Methods for Navier-Stokes Equations* (Springer-Verlag, Berlin, 1986).

[37] G. Matthies and L. Tobiska, Computing **69**, 119 (2002).

[38] V. John and G. Matthies, Int. J. Numer. Methods Fluids **37**, 885 (2001).

[39] V. John, Int. J. Numer. Methods Fluids **40**, 775 (2002).

[40] V. John, *Large Eddy Simulation of Turbulent Incompressible Flows. Analytical and Numerical Results for a Class of LES Models*, Lecture Notes in Computational Science and Engineering (Springer-Verlag, Berlin, 2004) Vol. 34.

[41] V. John and G. Matthies, Comput. Visualiztion Sci. **6**, 163 (2004).

[42] M. Schröter, K. Kassner, I. Rehberg, J. Claret, and F. Sagues, Phys. Rev. E **65**, 041607 (2002).